CFD modelling of convective falling films for enhanced algae cultivation: Fluid mechanics influence of mass transfer

Gerald Lancaster [1], *Bradley D.* Bock[1*] and *Ken J.* Craig[1]

[1]Clean Energy Research Group, Department of Mechanical and Aeronautical Engineering, University of Pretoria, Pretoria, South Africa

Abstract. Falling film photobioreactors are able to increase the mass transfer rates per volume of liquid through the gas-liquid interface compared to other photobioreactor types. At low Reynolds numbers the flow mass transfer is still diffusion limited. This work aims to resolve and improve the convective mixing within thin falling films numerically to optimize the rates of CO_2 absorption into a thin falling water film. Flat plate models are compared and it is found that slower films with a Reynolds number of 28 outperform faster flowing films by up to 2.5 times.

1 Introduction

Microalgae is now recognized as a biosource with high industrial potential for its applications in green chemistry and especially in the fields of food, biofuel, and the treatment of wastewater [1] as well as pharmaceutical products, cosmetics and aquaculture industries [2]. The effective scaling of its production cost is however still a challenge as most studies of microalgae production are usually conducted at a laboratory scale (less than 1 litre in volume), and therefore the cultivation and robustness of large-scale cultures remain very technically demanding, especially at low cost [3].

A photobioreactor (PBR) can produce up to 30 times more biomass concentration when compared to traditional raceway reactors, this higher production rate leads to lower recovery cost per quantity of biomass [4]. The use of thin liquid films influenced by gravity along a solid surface has seen its use in industrial processes like condensers, vertical tube evaporators, wetted wall absorbers and falling-film chemical reactors [5]. The development of a thin-film solar photobioreactor by [3] made use of the falling film principle to achieve very thin algal culture depths (1.5-2 mm). The increased biomass productivity of 5.7 $kg \cdot m^{-3} \cdot day^{-1}$ led to the further investigation of falling-film photobioreactor. Thin falling films have been observed to have rapid heat and mass transfer due to their micron-scale sized [6], and the efficiency of these systems are attributed their high specific interfacial area relative to their volume [7].

This study focuses on the physics involved in convective falling films and how the observed physical phenomena in falling-films can be utilised to enhance the production of microalgae in a falling-film photobioreactor. Thin falling films have become an attractive production method for PBRs due to their high rates of mass transfer, allowing high CO_2-absorption rates [8], and good lighting, preventing two common algae growth limiting factors [2].

Computational Fluid Dynamics (CFD) can be used to accurately model convective falling-film systems to economically test various geometries and flow rates to determine the characterization and quantification of the mass transfer coefficients associated with CO_2 absorption to ensure optimal conditions for algal growth.

The effects of internal motion and surface waves on the mass transfer rates at the gas-liquid interface have been found to be important [7],[9]. CFD has proven to be a valuable tool to investigate these effects. [10] investigated the effects of recirculation by directly solving the Navier-Stokes equations by means of the Volume of Fluid (VOF) numerical framework. This revealed the importance of the gas-liquid interface in wave formation. They found backflow, the internal circulation within the liquid film caused by the curvature of waves, resulted in a pressure gradient in the liquid film. [10] further found that this backflow led to improved mixing of the bulk fluid. Surface modifications can further have a positive effect on the mass transfer coefficient of a falling film. [11] performed both experimental and numerical simulations on flat plates with micro baffles. The purpose of these baffles was to introduce swirling patterns and recirculation zones within the liquid film, also referred to as convective mixing. They found that a baffled plate could form noticeably wavy and deformed quasi-stable falling films. In a follow-up study, [6] modelled the flow distributions within a convective falling film for a deeper investigation into the internal flow characteristics that led to enhanced mass transfer. Using different baffle layouts, the CO_2 absorption into water

* Corresponding author: bradley.bock@up.ac.za

was investigated numerically. They found that alternating baffles at 45^o managed to achieve an increase of 61% when compared to a standard smooth plate. Using wavy micro channels, the effects of wave structure and internal eddy flow on the enhancement of turbulence within a liquid film was investigated by [12]. They found that the film over a modified surface had a 41% increase in mass transfer when compared to a smooth surface. Work performed by [13] used the VOF method to investigate the effects of microstructures, liquid properties and gas flow rates on falling film flow behaviour. In their work it was found that in the absence of forced gas flow, wavy patterns mostly depend on the microstructure of the plate, and that proper micro structuring of the plate surface will lead to the formation of a continuous liquid film. When liquid properties are considered, it was found that surface tension has the most significant effect on flow patterns. Most of these early studies were purely done in the two-dimensional domain, and [14] was among the first to resolve a thin falling film in three-dimensions. Modelling a single wave, they explored the effects of spanwise wave features which were not previously resolved in two-dimensional studies. In their work, they showed the feasibility of accurately predicting wave structures in three-dimensional analysis.

This paper will first discuss the mathematical modelling of falling films and species transfer in **Section 2,** then the numerical solution strategy employed in **Section 3**. This is followed by validation of the hydrodynamic numerical model in **Section 4** and the species transfer validation in **Section 5**. The concluding remarks are presented in **Section 6.**

2 Mathematical modelling / Numerical simulation

2.1 Governing equations

For film flow, the mass and momentum conservation equations are as follows:

$$\frac{\partial \rho}{\partial t} + \nabla \cdot (\rho\, \vec{v}\,) = 0 \tag{1}$$

$$\frac{\partial (\rho \vec{v})}{\partial t} + \nabla \cdot (\rho \vec{v} \vec{v}) = -\nabla p + \nabla \cdot [\mu(\nabla \vec{v} + \nabla \vec{v}^T)] + \rho \vec{g} + \vec{F}_{vol} \tag{2}$$

where $\vec{F}_{vol}$, t , $\vec{v}$, p , and $\vec{g}$ are additional body force, time, velocity vector, pressure and gravitational acceleration respectively, while μ and ρ are the dynamic viscosity and density of the liquid.

By using the Continuum Surface Force (CSF) approach proposed by [15], we can find the additional forces on the system to only be applied at the free surface as

$$\vec{F} = \sigma \frac{\rho \kappa \alpha_L}{\left(\frac{1}{2}\right)(\rho_L + \rho_G)} \tag{3}$$

where σ and κ represent the surface tension coefficient and the curvature of the interface, respectively. κ can be defined as

$$\kappa = \nabla \cdot \frac{\vec{n}}{|\vec{n}|} = -\frac{1}{|\vec{n}|}\left[\frac{\vec{n}}{|\vec{n}|} \cdot \nabla |\vec{n}| - \nabla \cdot \vec{n}\right] \tag{4}$$

where $\vec{n}$ is the normal vector of the interface.

The VOF method as implemented in Ansys Fluent calculates the transport equation of phase fractions and thus for calculating physical properties uses a weighted average value at the interface:

$$\frac{\partial (\alpha_L \rho_L)}{\partial t} + \nabla \cdot (\alpha_L \rho_L \vec{v}_L) = 0 \tag{5}$$

$$\rho = \alpha_L \rho_L + (1 - \alpha_L)\rho_G \tag{6}$$

$$\mu = \alpha_L \mu_L + (1 - \alpha_L)\mu_G \tag{7}$$

$$\alpha_L + \alpha_G = 1 \tag{8}$$

where α represents the phase fraction. Subscripts G and L are used to indicate the gas and liquid phase respectively.

The volume fraction is used to track the interface between gas and liquid. For two phases, mass conservation becomes

$$\frac{1}{\rho_q}\left[\frac{\partial}{\partial t}\left(\alpha_q \rho_q\right) + \nabla \cdot \left(\alpha_q \rho_q \vec{v}_q\right) = S_{\alpha_q} + \sum_{p=1}^{n}\left(\dot{m}_{pq} - \dot{m}_{qp}\right)\right] \tag{9}$$

where $\dot{m}_{qp}$ is the mass transfer from phase q to phase p and $\dot{m}_{pq}$ is the mass transfer from phase p to phase q. By default, the source term S_α_q is zero but can be specified to be a constant or user-defined mass source for each phase.

2.2 Species transport equation

In order to quantify the mass transfer of CO_2 into a falling film, the species transport equation is solved. Ansys Fluent predicts the local mass fraction of each species, Y_i, by solving the convection-diffusion equation shown in Eq. (10) for the i^{th} species. The conservation equation as per [16] takes the general form of

$$\frac{\partial}{\partial t}(\rho Y_i) + \nabla \cdot (\rho \vec{v} Y_i) = \nabla \cdot \vec{J}_i + R_i + S_i \tag{10}$$

where ρ , $\vec{v}$, R_i and S_i are the density of the mixture, the velocity of diffusing species, the net rate of production of species i by chemical reaction, and the rate of creation by addition from the dispersed phase,

respectively. In Eq. (10) $\vec{J}_i$ is the diffusion flux of species i which arises due to gradients of concentration and temperature. Ansys Fluent by default uses a dilute approximation, called Fick's Law, to model mass diffusion. The Diffusion flux can be written as

$$\vec{J}_i = -\rho D_{i,m} \nabla Y_i - D_{T,i} \frac{\nabla T}{T} \qquad (11)$$

where $D_{i,m}$,Y_i , $D_{T,i}$ and T are the mass diffusion coefficient for species i in the mixture, mass fraction of species i, thermal (Soret) diffusion coefficient and temperature, respectively.

2.3 Boundary and initial conditions

A plate with small rectangular baffle was used for validation to allow for easy creation of a rectangular structured mesh. An inlet condition was defined as 0.2 mm thick for the incoming liquid film, with the air region adjacent to it being large enough to allow for the formation of the wavy interface. This region could be altered to reduce the computational domain size, thus reducing the cost of simulation, depending on the flow conditions (larger waves require a larger domain). For validation, the typical domain as mentioned by [11] of 1.8 mm for the gas inlet was used.

The liquid outlet was set to be the same size as that of the liquid inlet; this leads to an abnormal last wave and thus why some of the fluid domain at the outlet will be ignored in future analysis. The outlet boundary condition is changed from a pressure outlet to a velocity boundary condition with flow in the opposite direction to the velocity inlet; thus the velocity magnitude of liquid at the inlet is equal to the velocity flowing out at the outlet.

The side wall above the gas inlet is set to a slip wall as it would be open to the environment, while the contact wall is set to no-slip wall conditions.

Table 1. Boundary conditions.

Location	Boundary condition type	Reverence value
Fluid Inlet	Velocity Inlet	0.025 m/s, α_L=1
Gas Inlet	Velocity Inlet	0 m/s, α_L=1
Fluid Outlet	Velocity Inlet	-0.025 m/s, α_L=1
Gas Outlet	Pressure Outlet	0 PA Gauge Pressure, no backflow
Top Wall	Wall	Slip Wall (no shear)
Contact Wall	Wall	No Slip
Baffles	Wall	No Slip
Domain length	X-direction	40 mm
Domain height	Y-direction	2mm (0.2 and 1.8mm for liquid and air)

The boundary conditions from ***Table 1*** are shown in ***Fig. 1*** To implement the boundary conditions, a Journal file was created to enable Ansys Fluent to implement the method for each iteration automatically.

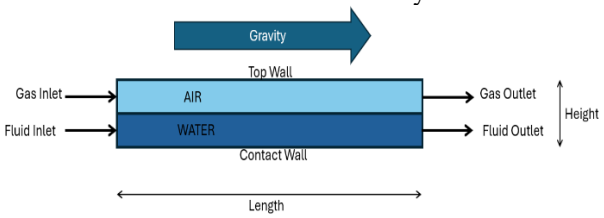

Fig. 1 : Schematic of domain with boundary conditions.

3 Numerical solution strategy

The solution strategy employed is similar to the method presented by [17], which involves comparing the accuracy of first solving the multiphase solution using the VOF method, and then implementing the stationary method on the now-calculated wavy gas-liquid interface, as initially proposed by [18]. For the second solution strategy they used a sub-grid scale (SGS) model as was shown by [19]. The two methods compared well to each other and theoretical solutions, thus the Stationary method was chosen for this work due to the higher computational expense of the SGS VOF method.

3.1 Hydrodynamics solver setup

As mentioned in [11], falling-film flow is fundamentally regarded as a time-dependent simulation. Thus, Ansys Fluent was set to perform a transient multiphase solution on the specified domain as shown in ***Fig. 2***. During the solution it is critical to have a sufficiently small time step relative to cell size, thus the adaptive time step method was used with a Courant number always kept between 0.25 and 0.5 to help ensure numerical stability. With the boundary conditions from ***Table 1*** defined in the simulation, the Hybrid Initialization function was used to initialize the domain to be solved. To improve the start-up procedure of the simulation it was found to be good practice to patch the initial liquid domain, as liquid. This step not only helped for reliability but also aided in solution times. From here the solution had to be run until quasi-steady state was reached, this occurs when waves don't change their shape and amplitude between timesteps, more on this in **section 4.2.1**.

The Pressure Implicit with Splitting Operators (PISO) scheme was selected for the pressure-velocity coupling as has been shown in the works of [11] and [20], along with the Pressure Staggering Option (PRESTO!) scheme for pressure interpolation. The second-order upwind scheme was adopted for convective terms and least squares cell-based algorithm for the velocity gradients. Using the Geometric Reconstruction Scheme (Geo-Reconstruct) aided in capturing of the gas-liquid interface.

3.2 Mesh independence

To evaluate the effects of cell sizing, a mesh independency study was performed on the computational domain. The accuracy of each mesh was based on its comparison to the reference value in [6], who obtained a film thickness of 174μm at a Reynolds number of 55.

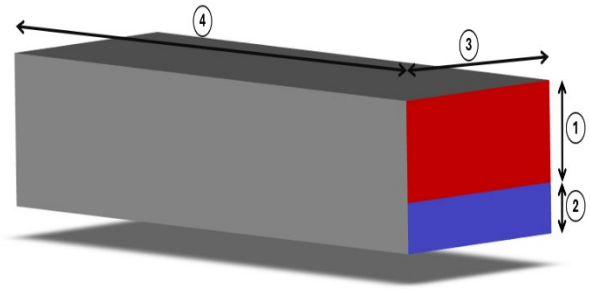

Fig. 2 Computational domain with numbered edges defined in Table 2.

Table 2. Mesh sizes as per numbered side

1	2	3	4
2×10^{-5}	1.5×10^{-5}	1.5×10^{-4}	1.5×10^{-4}
2×10^{-5}	2×10^{-5}	1×10^{-4}	1×10^{-4}
2×10^{-5}	1×10^{-5}	1×10^{-4}	1×10^{-4}
1×10^{-5}	1×10^{-5}	5×10^{-5}	5×10^{-5}

It can be seen in ***Table 3*** and in ***Fig. 3*** the finest mesh shows good agreement between the reference case of [6] and this work. The absolute percentage errors for the different meshes are shown in **Table 4**. The number of cores used at the Centre for High Performance Computing (CHPC) is also listed for each mesh. In ***Fig. 3***, the influence of the outlet condition can clearly be noted, it is for this reason that a sufficiently large portion of the liquid domain is discarded when comparing results.

Table 3. Mesh independence results.

Cell Count	Film Thickness [μm]	% Error
64080	172.2	1.03
144000	172.3	0.98
192000	173.4	0.34
1152000	174.1	0.03

This does show that the higher cell count simulations did perform the closest to [6]. However, when using only 192000 cells, which equates to 16.67% of the cell count of the finest mesh, the result is still within 1% of the reference value. Seeing as the more cells there are the more computationally expensive the simulation becomes; 192000 cells would be sufficiently accurate while being significantly more time efficient. Looking at the computational metrics (shown in ***Table 4.***), it can be noted that the additional accuracy comes at the cost of days in additional CPU time. 192000 cells are therefore used for the remaining simulations.

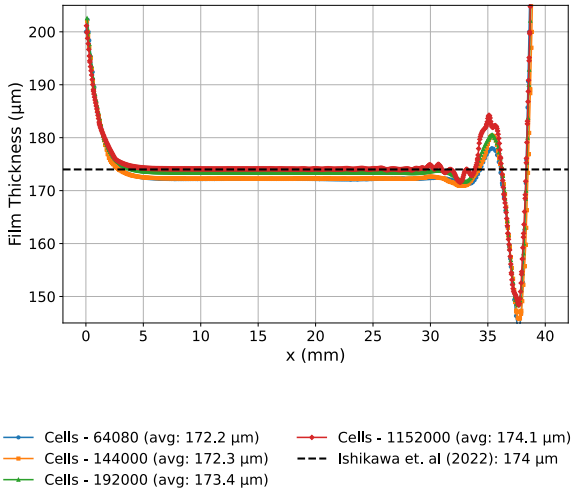

Fig 3. Mesh validation for film thickness

Table 4. Computational metrics for simulation at the CHPC

Type	Cores	Cell Count	CPU Time [days]	% Error
VOF	48	64080	5.79	1.03
VOF	48	142000	6.76	0.98
VOF	48	192000	9.12	0.34
VOF	96	1152000	11.84	0.03

3.3 Species concentration method solver

The Stationary method takes the gas-liquid interface solved in section 3.1 by means of the VOF method as input. The interface is now used as the side wall of the domain, acting as the boundary condition through which CO_2 absorption will occur. The method allows for the reconstruction of the computational domain, removing the need to use the VOF method to continuously track the gas-liquid interface. This method described by [17],[6], and [20] solves a steady-state solution of the species transport equation. The method makes use of a slip wall on the gas-liquid interface which is set to have a CO_2 mass fraction equal to that of the saturation concentration of air into water as calculated by Henry's Law.

The solution method uses the SIMPLE method for pressure velocity coupling, along with the PRESTO! scheme for pressure interpolation. The second-order upwind scheme was once again adopted for the convective terms.

4 Model hydrodynamic validation

4.1 Benchmark case

As part of the validation strategy, the study by [11], which investigated wavy falling films on micro-baffled plates, was identified as a suitable benchmark. Their work involved both experimental and numerical characterization of falling-film behaviour, focusing on flow patterns, wave structures, amplitudes of the waves, and film thicknesses. Their findings demonstrated strong agreement between numerical simulations and experimental measurements across a range of geometric configurations, flowrates and liquids. It is due to this, and the detailed images provided, that [11] has been chosen as the main benchmark to compare simulated results to.

4.2 Validation metrics

This comparison involves both qualitative and quantitative assessments of interface evolution and film properties as discussed in the following.

4.2.1 Interface evolution over time

Interface profiles at various timesteps (0.05 s, 0.1 s, 0.2 s, 0.3 s, and 0.5 s) were compared against those published by [11]. The interface was extracted at VOF=0.5 and plotted for each timestep. In the reference case of [11] detailed gas-liquid interface details for methanol flowing down a baffled plate, at a velocity of 0.025 m/s under gravity were given. Our PBR work deals with water, and [11] has averaged values for water but the most hydrodynamic details are given for methanol thus it serves as the metric for hydrodynamic validation of the model at low Reynolds Numbers (21-42). The 2D domain considered in this case is shown in ***Fig. 4***.

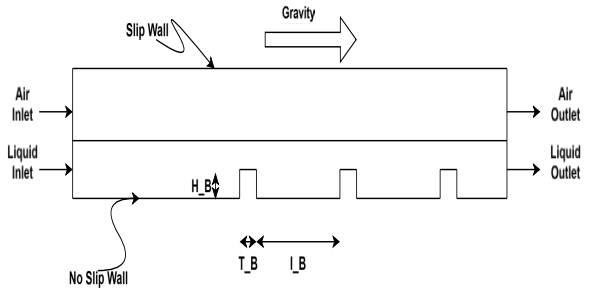

Fig. 4. Reference computational domain of Plate C similar to [11]

Table 5. Validation plates from [11]

Plate type	Baffle interval I_B [mm]	# Baffles	Total Plate Length [mm]
A	1	15	21
B	2	6	22.2
C	3	6	22.2
D	4	5	24
E	5	5	29

Table 5 outlines the plate dimensions, all plates considered made use of H_B= 0.1 mm and T_B = 0.2 mm. As reported in [11], the quasi-steady gas-liquid interface condition is reached by 0.3 s. In order to compare the simulation to the reference values, the average film thickness between 5-15 mm in the flow direction is compared, this is done to neglect the influences of inlet and outlet boundary conditions. ***Fig. 5*** shows how the simulated results from this work compare to [11]. A similar trend in the flow pattern can clearly be observed on the interface. It can also be observed that the comparison improves with simulation time, this shows that the quasi-steady state is being obtained and enables the use of the steady-state species concentration method described in **Section 3.3** as the interface resolves into a quasi-steady state wave form.

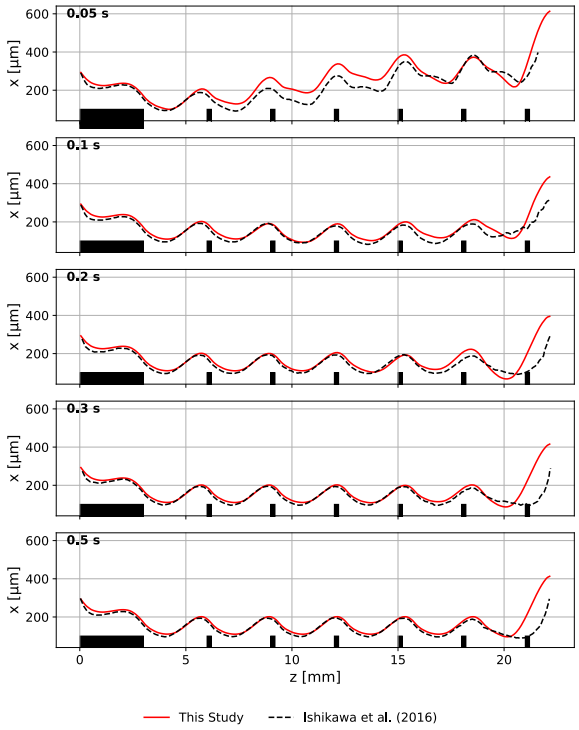

Fig. 5 Transient film thickness comparison to [11]

4.2.2 Wave-by-wave comparison

The flow domain was segmented based on individual wave positions (measured relative to the trailing edge of each baffle) and the morphology of each wave shape is compared. Due to the defined inlet and outlet conditions outlined in ***Table 5***, we are expecting the first and last wave to be disregarded. From ***Fig. 6***. it can be noted that wave numbers 2-6 line up near perfectly, with wave 1 out of sync as was expected due to the inlet condition's effect.

Fig.6 shows all five waves considered agree in phase, shape, amplitude and film thickness, a clear indication that the film reached steady state after 0.5 s of flow time.

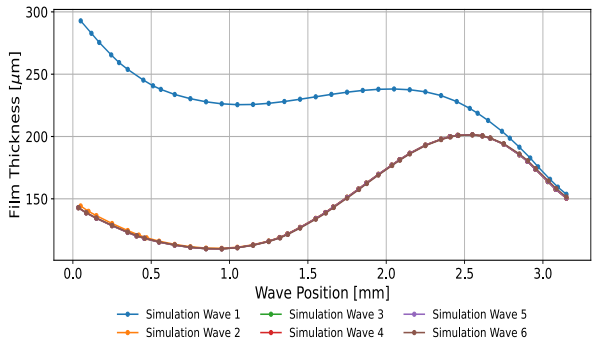

Fig. 6 Wave comparisons

4.3 Error and sensitivity analysis

The wave amplitude and film thickness at a specified downstream range were averaged in the flow direction (z = 5mm to 15mm), extracted and compared against experimental results from [11].

The geometries evaluated during this analysis are outlined in ***Table 5***, while the fluid properties are shown in ***Table 6.*** This allows us to investigate the robustness of our model over various configurations, in this case geometric and fluid property changes allow the effects of each property to also be considered.

The properties used in ***Table 6*** are of importance as surface tension (σ), density (ρ) and dynamic viscosity (μ) all play a defining role in the dimensionless Kapitza number (shown in **Eq.(12)** which is used to determine hydrodynamic regime of a falling liquid film, and further used to predict stability of the film [21].

$$Ka = \frac{\sigma}{\rho(g sin\mathrm{B})^{\frac{1}{3}}\nu^{\frac{4}{3}}} \qquad (12)$$

Table 6 Validation liquid properties [11]

Solvent	**Dynamic Viscosity** $\boldsymbol{\mu[Pa \cdot s]}$	**Density** $\boldsymbol{\rho\left[\frac{kg}{m^3}\right]}$	**Surface Tension** $\boldsymbol{\sigma\left[\frac{N}{m}\right]}$
Water	0.001	998	0.072
Methanol	0.0055	785	0.022
Ethanol	0.0012	790	0.022

In ***Fig. 7*** and ***Fig. 8***, the colours denote which fluid is being used (as defined in ***Table 6***), while the shapes denote the flow velocity, with circles representing an inlet velocity of 0.025 m/s and squares 0.1 m/s, respectively. The current work is represented with filled symbols while the numerical work of [11] is shown in open symbols. It should be noted that for both ***Figures 7, 8*** and **Tables 7, 8**, the values for [11] were not clearly stated and obtained by means of plot-digitization, which could lead to minor inaccuracies.

4.3.1 Average film thickness comparison

Looking at the average film thickness comparison in Figure ***Fig. 7*** between the results of this study and those of [11], it is evident that the predicted film thicknesses are generally in line with the validation data, with CFD results slightly overpredicting the film thickness in some cases. The percentage difference between the average film thickness solution obtained in the current work and that of [11] is summarized in ***Table 7***. Here we note that the largest difference occurs for Plate A and Plate B. The only difference on these plates is a smaller gap between individual baffles with these two cases having the smallest gaps.

However, the general shape of the predicted results does seem to follow the trends noticed in [11] with higher film thicknesses at the plates with a smaller interval between baffles and overall thicker liquid films at higher flowrates. It can also be noted that for both flow rates and all plates a clear trend of ethanol having the thickest film thickness while methanol has the thinnest film thickness can be observed. With the main difference between ethanol and methanol being dynamic viscosity it can further be said that dynamic viscosity has a significant effect on average film thickness in thin falling films

.

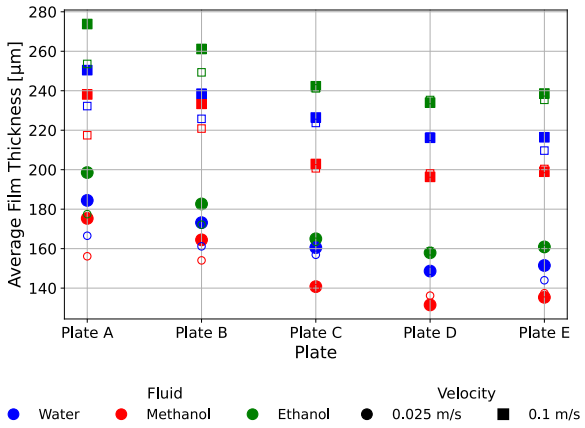

Fig. 7 Film thickness comparison to [11]

Table 7 Film Thickness percentage difference to [11]

		A	B	C	D	E
0,025 m/s	**Ethanol**	21.1%	10.5%	1.5%	0.7%	1.0%
	Methanol	19.2%	10.4%	0.8%	4.7%	2.1%
	Water	17.9%	12.0%	3.6%	0.2%	7.5%
0,1 m/s	**Ethanol**	20.2%	11.8%	1.1%	1.3%	2.0%
	Methanol	20.7%	12.5%	2.2%	1.7%	1.4%
	Water	18.2%	12.7%	2.3%	0.5%	6.0%

4.3.2 Amplitude comparison

Using the same validation plates and fluid properties outlined in ***Tables 5, 6*** the amplitudes of the resulting waves were compared to the work of [11]. Looking at the results in ***Fig. 8*** it can be noted that the results of amplitude compare much closer to the results obtained by [11] than the film thicknesses shown before.

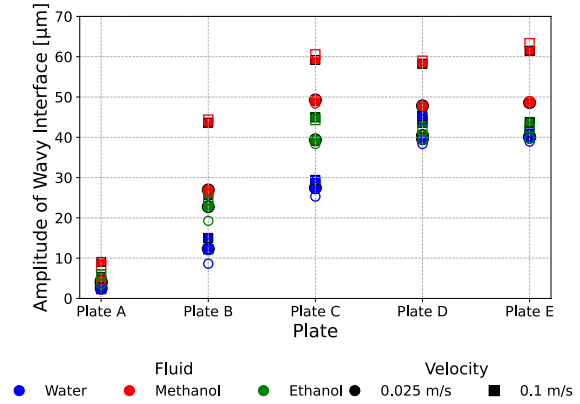

Fig. 8 Amplitude comparison to [11]

This is confirmed in ***Table 8*** where the percentage difference between the current work and that of [11] shows the largest difference between the current works amplitude and that of [11] being only 3.7%.

It can be noted that as the distance between baffles gets larger there is a noted increase in the amplitude with Plate A (the smallest interval) having the smallest wave over all solvents and velocities.

Table 8 Amplitude Percentage difference to [11]

		A	B	C	D	E
0,025 m/s	**Ethanol**	0.2%	3.5%	1.0%	1.0%	0.5%
	Methanol	0.2%	0.8%	0.9%	0.0%	0.4%
	Water	0.2%	3.7%	2.2%	1.3%	1.0%
0,1 m/s	**Ethanol**	0.6%	1.3%	0.7%	1.8%	1.4%
	Methanol	0.8%	0.7%	1.4%	0.9%	1.9%
	Water	0.1%	2.8%	0.9%	0.9%	0.4%

4.3.3 3D Validations

As [11] dealt only with 2D cases, the hydrodynamics of the 3D work performed in [11] was used to validate the 3D solutions in the current work. As minimal 3D flat plate cases were reported, a selection of the horizontal baffled cases were used to further validate the 3D solver in the current work, results and configuration shown in ***Fig. 9*** and ***Table 9*** and ***Table 10.*** [11] is more mass transfer focused and thus only reports average film thicknesses to at a selection of falling film options.

Table 9 Setup conditions for 3D validation

Case	Width [mm] (3) in Fig. 2	Re	Simulation Time [s]
1	1,2	55	0,5
2	0,8	55	0,5
3	1,8	55	0,5
4	2,4	55	0,5
5	1,2	28	0,5
6	1,2	84	0,5
7	1,2	111	0,5
8	1,8	55	0,8
9	2,4	55	1,2
10	1,2	28	1

Table 10 3D Validation results compared to[6]

Case	Film thickness [μm]	Reference [μm]	% Difference
1	222,94	224	0,47
2	227,94	232	1,78
3	219,71	222	1,05
4	214,84	221	2,87
5	183,86	190	3,34

6	249,25	252	1,11
7	273,21	277	1,37
8	221,25	222	0,34
9	214,93	221	2,82
10	190,21	190	0,11

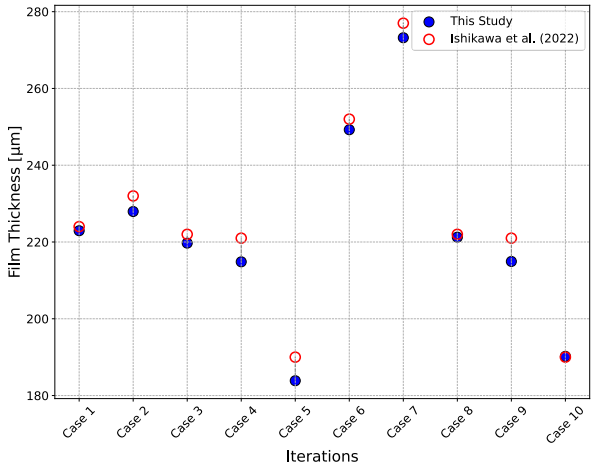

Fig. 9 3D Film thickness comparison to [6]

In ***Fig. 10*** and ***Table 11*** the 3D results of [6] correspond with the values in this current study for the flat plate cases given. It can also be seen that with 192000 cells when the Reynolds number is varied (Re = 28 ,55, 111), the simulation remains within 1% of the values given by [6].

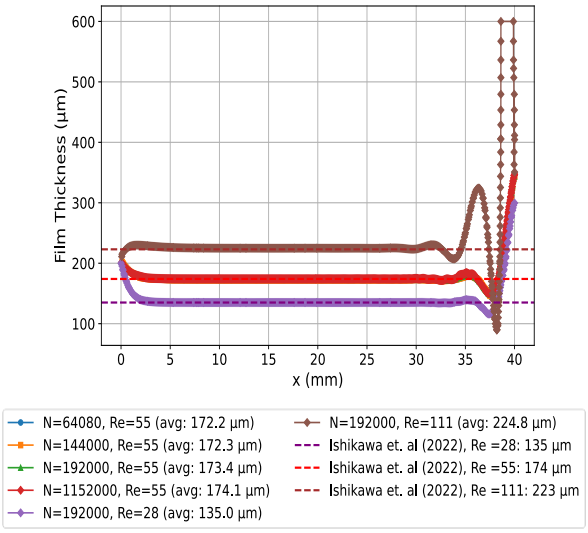

Fig. 10 3D Flat plate film thickness comparison to [6]

Table 11 Validation of 3D liquid film thickness compared to [6]

Re	Cell Count	Film thick-ness [μm]	Reference film thickness [μm]	% Error
28	192000	135	135	0
55	64080	172.2	174	1.03
55	144000	172.3	174	0.98
55	192000	173.4	174	0.34
55	1152000	174.1	174	0.06
111	192000	224.8	223	0.81

5 Mass transfer model validation

5.1 Method

After performing the hydrodynamic analysis on a flat plate at different flow rates (Re = 28, 55, 111) and verifying that the film thickness for each is correct and in line with literature reported in [6], the computational domain shown in ***Fig. 2*** was altered by using the process illustrated in **Fig 11.**

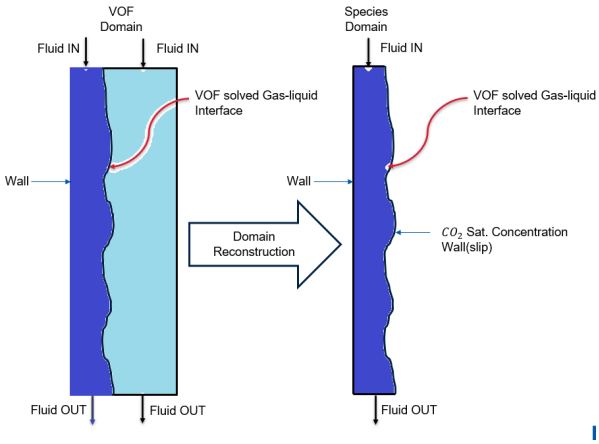

Fig 11 Computational domain reconstruction

The species transport method outlined in **section 3.3** was solved on flat plates with Reynolds numbers (Re = 28, 55, 111).

The mass transfer coefficient is the calculated along the film flow length by

$$k_L = \frac{Q}{W\,z}\ln\left(\frac{C_{CO_2,sat}}{C_{CO_2,sat} - C_{CO_2,z}}\right) \qquad (13)$$

where k_L is the mass transfer coefficient in $[m/s]$, Q is the volumetric flow rate in $[m^3/s]$, W is the width of the computational domain (number 3 in ***Fig. 2***), z is the length down the falling film to the measurement point. $C_{CO_2,sat}$ is the CO_2 molar concentration at the saturated interface and $C_{CO_2,Z}$ is the CO_2 molar concentration at the measurement point.

5.2 3D Validation

The percentage difference between the simulation produced in this work compared to the values reported in Ishikawa *et al.* [6] are outlined in ***Table 12***, the largest difference (15.81%) occurs at a Reynolds number of 55 on the simulation with the finest mesh. This is most likely due to the method in which the computational domain is restructured, as the reconstruction of the gas-liquid interface is not a smooth surface, the sides of the cells contained in waves at the gas-liquid interface cause a larger mass transfer area. This is confirmed in ***Table 13*** where for the simulations of Re=55 the largest cell count simulation also has the largest gas-liquid interfacial area. A smooth gas-liquid interface should be considered and compared to the current solution. Mesh statistics for the species transport simulation are reported in **Table 13**.

Table 12 Mass transfer coefficient compared to Ishikawa *et al.* [6]

	Re	Reference $k_L \times 10^4$ $[m/s]$	This Study $k_L \times 10^4$ $[m/s]$	% Difference
Flat	28	1,82	1,58	13,39
	55 A	1,05	0,918	12,56
	55 B	1,05	0,90	14,68
	55 C	1,05	0,91	13,06
	55 D	1,05	0,88	15,81
	111	0,61	0,64	4,92

Due to the mass transfer coefficient continuously changing throughout the domain, Ishikawa *et al.* [6] only reported a mass transfer coefficient at a single point along the length of the plate in their domain (z = 28mm from the point where $C0_2$ absorption starts). With this in mind, this study reports on the average mass transfer coefficient up to each point across the entire plate length to gather more insights into which properties have the largest effects on mass transfer enhancement.

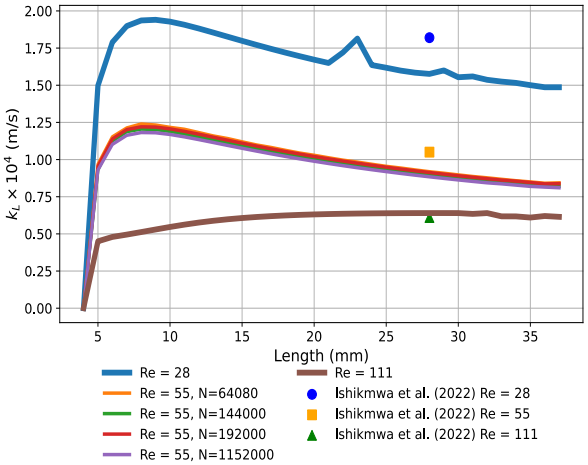

Fig 12 Mass coefficient k_L along plate length

In ***Fig 12*** it can be noted that the lower the Reynolds number, the higher mass transfer coefficient is predicted. Also noted is the initial spike in mass transfer that then flattens out as the flow continues along the flow domain. This spike appears to be more pronounced in slower flows than films with a larger flowrate.

Table 13 Species transport mesh statistics

Simulation	Cell Count	CO_2 Contact Area $\times 10^5$ $[m^2]$
Re = 28	495536	3.9801
Re =55 A	190592	3.6917
Re = 55 B	285312	3.9617
Re = 55 C	609888	3.9636
Re = 55 D	2285856	3.9677
Re = 111	793520	3.9826

Of the simulations with the same Reynolds number, we note in ***Table 13*** that the largest cell count simulation also has the largest interfacial surface area, thus it could be resolving smaller waves which are not possible to predict at the lower cell count meshes.

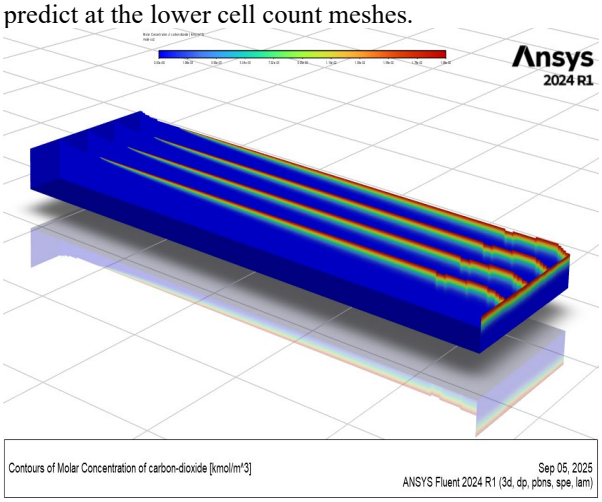

Fig. 13 CO_2 Absorption pattern (Scaled by a factor of 10 in flow direction)

In ***Fig. 13*** a contour plot of CO_2 molar concentration is displayed. It is evident that the CO_2 absorption occurs from the area in contact with the environment, however, the absorption region is very flat and thin, with no apparent bulk fluid mixing. With films as thin as $135\mu m$ there is still fluid not in direct contact with CO_2 which could hinder the growth of algae.

6 Conclusions

In this study, the CO_2 absorption into a thin falling-film liquid on a flat plate for use as a photobioreactor has been modelled using CFD. The proposed model was validated against literature and hence allows for further investigation of CO_2 absorption into thin falling films.

It was found that lower velocity films have a higher mass transfer coefficient than films with a higher flow rate, with Re = 28 performing 1.74 times better than a film with Re =55, and 2.5 times better than a film with Re =111. This is most likely because of the liquid having a longer residence time and thus more time in contact with the CO_2. As the lack of mixing in flat plat falling films cause no clear disadvantage, and mass transfer enhancement is primarily influence by resident time caused by lower flowrates.

It was also observed that the absorbed CO_2 concentration is primarily located at the gas-liquid interface, meaning that most of the bulk liquid has no interaction with the CO_2,this provides future research opportunity to improve, CO_2 absorption by mixing the bulk fluid using structured surfaces.

Acknowledgements

The authors acknowledge the Centre for High Performance Computing (CHPC), South Africa, for providing computational resources to this research project and the support of the Royal Society International Science Partnership Fund (ISPF) International Collaboration Awards (Award number ICAO\R1\241138).

Data availability

Data are available on request.

Author contributions

Gerald Lancaster: Conceptualization, Methodology, Validation, Formal analysis, Investigation, Data curation, Writing – original draft**.**
Bradley Bock: Conceptualization, Methodology, Resources, Supervision, Writing – review and editing
Ken Craig: Conceptualization, Methodology, Resources, Supervision, Writing – review and editing

References

1. Pruvost J, Rasheed R, Samhat K, et al (2024) A simple new approach predicting how microalgae culture systems will perform under sunlight and artificial light conditions. Algal Res 80:. https://doi.org/10.1016/j.algal.2024.103517
2. Bitog JP, Lee IB, Lee CG, et al (2011) Application of computational fluid dynamics for modeling and designing photobioreactors for microalgae production: A review. Comput Electron Agric 76:131–147. https://doi.org/10.1016/J.COMPAG.2011.01.015
3. Pruvost J, Le Borgne F, Artu A, Legrand J (2016) Development of a thin-film solar photobioreactor with high biomass volumetric productivity (AlgoFilm©) based on process intensification principles. https://doi.org/10.1016/j.algal.2016.10.012
4. Chisti Y (2007) Biodiesel from microalgae. Biotechnol Adv 25:294–306. https://doi.org/10.1016/j.biotechadv.2007.02.001
5. Xu ZF, Khoo BC, Wijeysundera NE (2008) Mass transfer across the falling film: Simulations and experiments. Chem Eng Sci 63:2559–2575. https://doi.org/10.1016/j.ces.2008.02.014
6. Ishikawa H, Ookawara S, Yoshikawa S, Matsumoto H (2022) Numerical study on mass

transfer in a falling film on structured plates with micro-baffles. Chemical Engineering and Processing - Process Intensification 175:108903. https://doi.org/10.1016/j.cep.2022.108903
7. Ho CD, Chang H, Chen HJ, et al (2011) CFD simulation of the two-phase flow for a falling film microreactor. Int J Heat Mass Transf 54:3740–3748. https://doi.org/10.1016/J.IJHEATMASSTRANSFER.2011.03.015
8. Chang H-C, Demekhin EA (2002) Chapter 1 - Introduction and History. In: Chang H-C, Demekhin EA (eds) Studies in Interface Science. Elsevier, pp 1–4
9. Albert C, Marschall H, Bothe D (2014) Direct Numerical Simulation of interfacial mass transfer into falling films. Int J Heat Mass Transf 69:343–357. https://doi.org/10.1016/j.ijheatmasstransfer.2013.10.025
10. Åkesjö A, Gourdon M, Vamling L, et al (2019) Modified surfaces to enhance vertical falling film heat transfer – An experimental and numerical study. Int J Heat Mass Transf 131:237–251. https://doi.org/10.1016/j.ijheatmasstransfer.2018.11.061
11. Ishikawa H, Ookawara S, Yoshikawa S (2016) A study of wavy falling film flow on micro-baffled plate. Chem Eng Sci 149:104–116. https://doi.org/10.1016/j.ces.2016.04.021
12. Chen X, Wang J, Lu T, et al (2022) Three-dimensional film thickness distribution of horizontal tube falling film with droplet and sheet flow. International Journal of Multiphase Flow 148:103933. https://doi.org/10.1016/J.IJMULTIPHASEFLOW.2021.103933
13. Gu F, Liu CJ, Yuan XG, Yu GC (2004) CFD Simulation of Liquid Film Flow on Inclined Plates. Chem Eng Technol 27:1099–1104. https://doi.org/10.1002/CEAT.200402018
14. Kahouadji L, Batchvarov A, Adebayo IT, et al (2022) A numerical investigation of three-dimensional falling liquid films. Environmental Fluid Mechanics 22:367–382. https://doi.org/10.1007/s10652-022-09849-2
15. Brackbill JU, Kothe DB, Zemach C (1992) A continuum method for modeling surface tension. J Comput Phys 100:335–354. https://doi.org/10.1016/0021-9991(92)90240-Y
16. (2024) Ansys Fluent Theory Guide January 2024 R1. Release 2024 R1
17. Xie H, Zong Y, Shen L, Dai G (2021) Interfacial mass transfer intensification with highly viscous mixture. Chem Eng Sci 236:. https://doi.org/10.1016/j.ces.2021.116531
18. Wasden FK, Dukler AE (1990) A numerical study of mass transfer in free falling wavy films. AIChE Journal 36:1379–1390. https://doi.org/10.1002/aic.690360911
19. Weiner A, Bothe D (2017) Advanced subgrid-scale modeling for convection-dominated species transport at fluid interfaces with application to mass transfer from rising bubbles. J Comput Phys 347:261–289. https://doi.org/10.1016/J.JCP.2017.06.040
20. He L, Xie H, Zong Y, et al (2025) Enhancing interfacial mass transfer for high-viscosity fluids: Hydrodynamic and mass transfer by twin-liquid film. AIChE Journal 71:. https://doi.org/10.1002/aic.18708
21. Mendez MA, Scheid B, Buchlin J-M (2017) Low Kapitza falling liquid films. Chem Eng Sci 170:122–138. https://doi.org/https://doi.org/10.1016/j.ces.2016.12.050